AIMS Energy, 9(1): 96–116.
DOI: 10.3934/energy.2021006
Received: 16 October 2020
Accepted: 14 December 2020
Published: 18 December 2020

http://www.aimspress.com/journal/energy

Research article

Influences of atmospheric water vapor on spectral effective emissivity of a single-layer radiative cooling coating

Cheng Ziming[1,2], Lin Bo[2], Shi Xuhang[2], Wang Fuqiang[1,2,3,*], Liang Huaxu[1,2] and Shuai Yong[1,3]

[1] School of Energy Science and Engineering, Harbin Institute of Technology, 92, West Dazhi Street Harbin 150001, P. R. China
[2] School of New Energy, Harbin Institute of Technology at Weihai, 2, West Wenhua Road, Weihai 264209, P. R. China
[3] Key Laboratory of Aerospace Thermophysics, Ministry of Industry and Information Technology, Harbin 150001, P. R. China

* **Correspondence:** Email: Wangfuqiang@hitwh.edu.cn; Tel.: +866315687210.

Abstract: Radiative cooling technology can emit infrared heat to the outer space through the "sky window" for cooling without consuming energy, which had drawn more and more attention. However, some researches reported that there was a significantly different cooling performance at different atmospheric total water vapor columns (TWC) conditions. In this study, taking a simple single-layer radiative cooling coating containing two kinds of particle mixture (SiO_2, TiO_2) as example, the spectral effective emissivity of the radiative cooling coating was proposed to evaluate the effect of the atmospheric water vapor on the cooling performance. The spectral effective emissivity of the coating was obtained through multiplying spectral emissivity of the coating by the atmospheric transmittivity, where the spectral emissivity was calculated by combining an algorithm for calculating radiative properties of the multi-particle system with the Monte Carlo ray-tracing method (MCRT). The effects of different atmospheric water vapor on the spectral effective emissivity of the simple single-layer radiative cooling coating containing different particles size, volume fraction and thickness were studied to improve the cooling performance of the coating. The results showed that with increasing TWC from 0 to 7000 atm-cm, the average effective emissivity of the simple single-layer coating decreased from 79.5% to 35.3%, with a decrease of 44.2%. The research results are of great significance to the further application development and the design criterion of radiative cooling materials in different atmospheric water vapor environments.

Keywords: radiative cooling; total water vapor column; radiative transfer; effective emissivity

Nomenclature: a_n: Mie scattering coefficients; b_n: Mie scattering coefficients; D: particle diameter, nm; f_v: particle volume fraction; G: projected area, m^{-2}; g: asymmetry factor; I: solar intensity; k: index of absorption; m: complex refractive index; n: index of refraction; N: number density of particles, m^{-3}; Q: efficiency factor; R: Reflectivity; RH: relative humidity; S_1: complex amplitude functions; S_2: complex amplitude functions

Greek symbols: λ: wavelength, nm; τ : Transmittivity; Θ : scattering angle; ε : emissivity; ω: scattering albedo; κ : absorption coefficient, m^{-1}; χ : size parameter; σ : scattering coefficient, m^{-1}; β : extinction coefficient, m^{-1}; ϕ : azimuth angle; Φ : scattering phase function; Ω : solid angle, sr; Θ: angle of incidence

Subscripts: abs: absorption; BB: blackbody; ext: extinction; P: particle; sca: scattering

1. Introduction

With the energy crisis and global warming, human beings were paying more attention to energy saving and emission reduction technology [1–4]. The building refrigeration system consumed approximately 20% of the global indoor electricity and accounted for 10% of the global greenhouse gas emissions [5,6]. The energy consumption of the air conditioner could be reduced by 3–5% for every 1 ℃ reduction of the temperature needed to be reduced. The daytime radiative cooling technology can reflect sun irradiation strongly and emitted infrared energy to the outer space through 'sky window', which could achieve several degrees of cooling below ambient temperature without consuming any additional energy [7–9]. This technology has very broad prospects, which could be applied in the fields of constructions, refrigerated vehicles and photovoltaic cells [10,11]. Radiative cooling technology had attracted many researchers to prepare high-performance radiative coolers [12–14].

In recent years, in order to obtain high-performance radiative cooling materials, researchers had done a lot of work on the design and preparation of films, nanoparticle-based coatings and photonic structure devices [15–20]. For example, Raman et al. 21 prepared a multi-layer photonic radiative cooler by magnetron sputtering HfO_2 and SiO_2. This radiative cooler achieved a cooling power of 40 W/m^2 and a sub-ambient temperature drops of nearly 5 ℃ under solar irradiation. Fan et al. proposed a radiative cooling foil composed of a fluorinated polyimide embedding SiO_2 microspheres. This radiative cooling foil achieved a cooling effect of 4.6 ℃ lower than ambient temperature. Cheng et al. 22 proposed a single-layer radiative cooling coating that the reflectivity (0.3–2.5 μm) and the emissivity (8.0–13.0 μm) were more than 0.95. Huang et al. 23 designed a double-layer radiative cooling coating that the top layer embedded with TiO_2 particles reflected 90% of solar irradiation and the bottom layer embedded with carbon black particles emitted 90% of infrared heat to the outer space.

The researchers designed high-performance radiative cooling materials, but the same material had a significantly different cooling performance when they were tested at different regions or weather conditions. Atmospheric water vapor was regarded as the most important factor affecting cooling performance of radiative cooling materials [23–27]. Zhai et al. 28 invented metamaterial containing glass particles for radiative cooling. This metamaterial could reflect 96% of solar radiation

and had a 93% average emittance in the 'sky window' region. The cooling power was 93 W/m^2 during daytime in Arizona on the dry autumn days (October 16–19). However, Ref. 29 which was published from the research group of Zhai et al. reported that daytime cooling power of the same material was only 45 W/m^2 when it was tested in Colorado on the moist summer day (August 31, relative humidity (RH) = 55%). Mandal et al. 30 manufactured a hierarchically porous polymer radiative cooling coating, which had 96% solar reflectivity and 97% infrared emissivity at 8–13 μm wavelengths. The outdoor experiments showed that the temperature drop of the coating was 6 ℃ under sunlight of 890 W/m^2 in arid Phoenix, while the temperature drop of the coating was only 4.5 ℃ under sunlight of 760 W/m^2 in coastal New York. Liu et al. 31 demonstrated a hierarchical porous cooling material having a solar reflectivity of 95% and long-wave emissivity of 95%. The temperature drop in dry season could reach 6 ℃, while it was only 2.7 ℃ in the humid season. Li et al. 32 did an detailed analysis of the contribution of atmospheric constituents (including water vapor) to the spectral values of the sky emissivity, and proposed correlations for the effective sky emissivity in several longwave bands as functions of the normalized ambient partial pressure of water vapor.

The literature survey indicated that many types of radiative cooling materials had been designed and prepared by researchers. However, practical applications of radiative cooling materials were seriously limited due to the high cost and complexity of preparation. Besides, the literature survey also indicated that the atmospheric water vapor was an important factor affecting the radiative cooling performance. But there was lack of an analysis from the aspect of spectral effective emissivity of the coating. In this work, taking a simple single-layer radiative cooling coating containing two kinds of particle mixture (SiO_2, TiO_2) as example, the spectral effective emissivity of the radiative cooling coating was proposed to evaluate the effect of the atmospheric water vapor on the cooling performance, as shown in Figure 1. The spectral effective emissivity of the coating was obtained through multiplying spectral emissivity of the coating by the atmospheric transmittivity, where the spectral emissivity was calculated by combining an algorithm for calculating radiative properties of the multi-particle system with the Monte Carlo method. The effects of different atmospheric water vapor on the spectral effective emissivity of coating containing different particles size, volume fraction and thickness were studied. The research results are of great significance to the further application development of radiative cooling materials in different atmospheric water vapor environments.

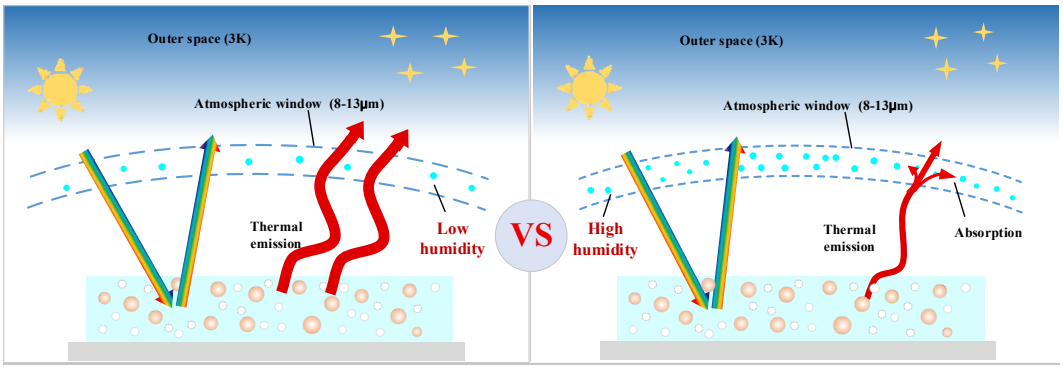

Figure 1. Schematic diagram of the influences of TWCs on cooling performance of the coating.

2. Theory and methodology

Figure 2 presented the basic procedures to calculate the radiative properties of the coatings by solving the radiative transfer equation (RTE). Firstly, the radiative properties of a single particle were calculated by Mie theory, such as extinction factor, asymmetry factor. Then, the radiative properties of the multi-particle system with non-uniform size were obtained by the algorithm developed by the authors. At last, the spectral reflectivity and emissivity of coatings consisting of base material and multi-particles were obtained by solving the RTE by Monte Carlo ray-tracing method.

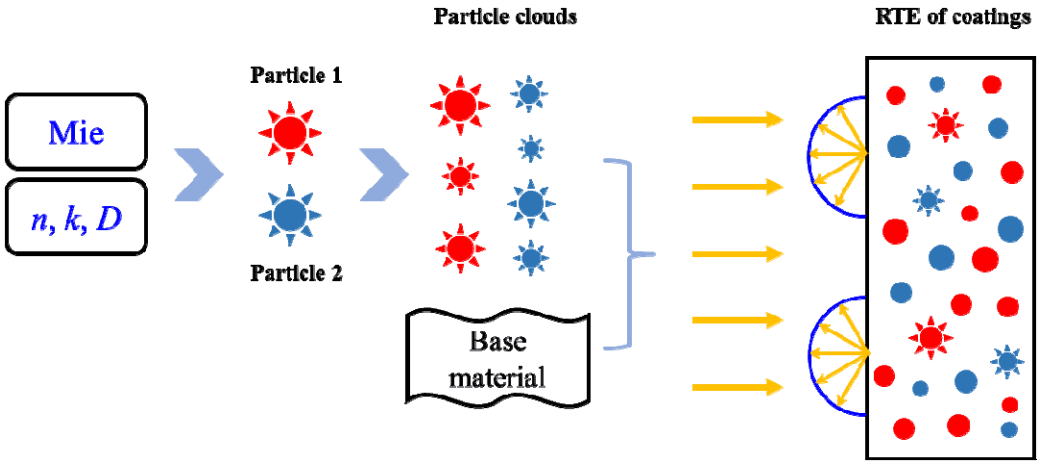

Figure 2. Basic procedures of the algorithm to calculate the optical properties of the coatings by solving the RTE.

2.1. Radiative properties of multi-particle system

The multi-particle system was composed of different kinds of particles with different sizes. The radiative properties of a single spherical particle, such as extinction efficiency factor Q_{ext}, scattering efficiency factor Q_{sca}, scattering phase function $\Phi(\Theta)$, asymmetry factor *g*, etc., were governed by two independent parameters: the size parameter $\chi = \frac{\pi D}{\lambda}$ and the complex refractive index $m = n - \mathrm{i}k$, where n represented the index of refraction and k represented the index of absorption [33–36]. The spectral complex refractive indexes of TiO_2 and SiO_2 at 0.3–15.0 μm wavelength were given in Figure 3 37. The Q_{ext}, Q_{sca}, $\Phi(\Theta)$, g and etc. can be calculated by Mie theory [33–36].

$$Q_{\text{ext}}(m,\chi) = \frac{2}{\chi^2}\sum_{n=1}^{\infty}(2n+1)\,\mathrm{Re}\{a_n + b_n\} \tag{1}$$

$$Q_{\text{sca}}(m,\chi) = \frac{2}{\chi^2}\sum_{n=1}^{\infty}(2n+1)\left(|a_n|^2 + |b_n|^2\right) \tag{2}$$

$$Q_{\text{abs}}(m,\chi)=Q_{\text{ext}}(m,\chi)-Q_{\text{sca}}(m,\chi) \tag{3}$$

$$\Phi(\Theta)=\frac{2}{\chi^2 Q_{\text{sca}}}\left[|S_1|^2+|S_2|^2\right] \tag{4}$$

$$g_{\text{p}}=\overline{\cos\Theta}=\frac{1}{4\pi}\int_{4\pi}\Phi_{\text{p}}(\Theta)\cos\Theta\,\text{d}\Omega \tag{5}$$

where Re represented the real component of the function, the symbol a_n and b_n represented the Mie scattering coefficients. The a_n and b_n were the Mie scattering coefficients. Θ was the scattering angle. The S_1 and S_2 were the complex amplitude functions.

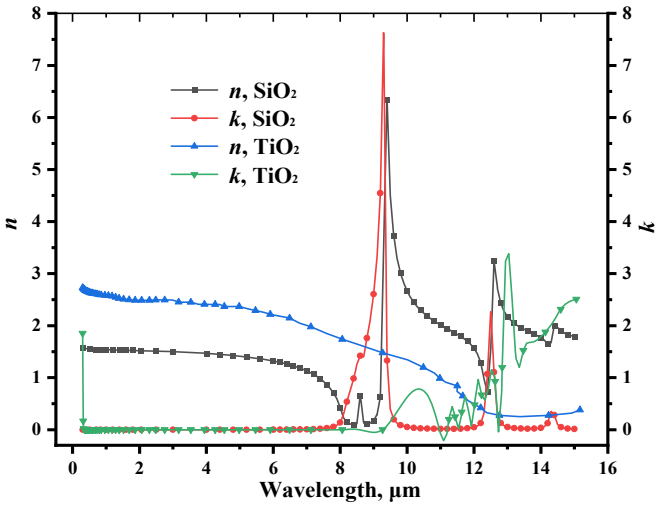

Figure 3. The complex refractive indexes of SiO_2 and TiO_2.

The extinction coefficient β, scattering coefficient σ_{s}, absorption coefficient κ were derived as [33–36]:

$$\beta=\sum_{i=1}^{n}\sum_{j=1}^{n_i}N_{i,j}C_{\text{e};i,j}=\frac{\pi}{4}\sum_{i=1}^{n}\sum_{j=1}^{n_i}D_{i,j}{}^2N_{i,j}Q_{\text{e};i,j}=1.5\sum_{i=1}^{n}\sum_{j=1}^{n_i}\frac{Q_{\text{e};i,j}f_{v;i,j}}{D_{i,j}} \tag{6}$$

$$\sigma_{\text{s}}=\sum_{i=1}^{n}\sum_{j=1}^{n_i}N_{i,j}C_{\text{s};i,j}=\frac{\pi}{4}\sum_{i=1}^{n}\sum_{j=1}^{n_i}D_{i,j}{}^2N_{i,j}Q_{\text{s};i,j}=1.5\sum_{i=1}^{n}\sum_{j=1}^{n_i}\frac{Q_{\text{s};i,j}f_{v;i,j}}{D_{i,j}} \tag{7}$$

$$\kappa=\beta-\sigma_{\text{s}} \tag{8}$$

where n represented the number of the particles, N represented the number density of the particles. The subscript i represented different kinds of particles and the subscript j represented different particle sizes. C_{e} represented the extinction area of the particles and C_{s} represented the scattering area

of the particles. The f_v represented the volume fraction of the particles.

The scattering phase function $\Phi(\Theta)$ of the multi-particle system was modified as:

$$\Phi(\Theta)=\frac{1}{\sigma_{\mathrm{s}}}\sum_{i=1}^{n}\sum_{j=1}^{n_i}\sigma_{\mathrm{s};i,j}\cdot\Phi_{i,j}(\Theta)=\frac{1}{\sigma_{\mathrm{s}}}\sum_{i=1}^{n}\sum_{j=1}^{n_i}\frac{Q_{\mathrm{s};i,j}f_{v;i,j}}{D_{i,j}}\cdot\Phi_{i,j}(\Theta) \tag{9}$$

The asymmetry factor g of the multi-particle system was calculated from:

$$g=\frac{1}{\sigma_{\mathrm{s}}}\sum_{i=1}^{n}\sum_{j=1}^{n_j}\sigma_{\mathrm{s};i,j}\cdot g_{i,j} \tag{10}$$

2.2. Solving the RTE by MCRT

The multi-particles were embedded in the acrylic resin (base material). The index of refraction of the acrylic resin was 1.5 and the index of absorption of it at 0.3–15.0 μm wavelength was much smaller, so it was treated as a non-absorbent medium. The RTE for describing the radiative transfer of the coating containing base material and multi-particle was written as followed and it was solved by using the MCRT method [33–36]:

$$\frac{\mathrm{d}I_\lambda(s)}{\mathrm{d}s}=-k_\lambda I_\lambda(s)-\sigma_\lambda I_\lambda(s)+k_\lambda I_{\mathrm{b}\lambda}(s)+\frac{\sigma_\lambda}{4\pi}\int_{4\pi}I_\lambda\left(s,\vec{\Omega}'\right)\Phi_\lambda\left(\vec{\Omega}',\vec{\Omega}\right)\mathrm{d}\Omega' \tag{11}$$

I_λ represented the spectral radiative intensity. $I_{\mathrm{b}\lambda}$ represented the spectral blackbody intensity. Ω represented the solid angle. The calculated result were the absorptivity, reflectivity and transmissivity of the coating itself.

The basic idea of the Monte Carlo ray tracing method was as following: When a photon bundle traveled in the coating, the bundle would be absorbed and scattered, and the free path length S can be expressed as:

$$\Delta S=-\frac{1}{\beta}\ln\xi_1$$

The symbol ξ_1 was a random number with a uniform distribution of 0–1. When the photon traveled, another random number ξ_2 ($0 < \xi_2 < 1$) to determine whether the photon was to be absorbed or scattered. The random number ξ_2 was compared with the scattering albedo $\omega=\delta/\beta$. If $\xi_2 > \omega$, the photon would be absorbed, otherwise the photon would be scattered. For more details about the MCRT, please refer to the papers 38.

2.3. Atmospheric total water vapor column (TWC)

There were many factors affecting the atmospheric transitivity (τ), such as H_2O, O_3, CO_2, CO and etc. As shown in Table 1, water vapor had a strong split emission band centered at 1.38, 1.87, 2.7, 6.3 and 71 μm, which affected the atmospheric transmittance in solar waveband and the 'sky window' region 33. The TWC was a method for measuring the total water vapor contained in a vertical column of the atmosphere 39. TWC was relevant to the absolute humidity and local temperature that is not under control. The correlation between the TWC and humidity could be calculated by the empirical table given in MODTRAN, as shown in Table 2. The larger relative humidity, the higher TWC. For example, TWC = 0 atm-cm (RH = 0%), 1000 atm-cm (RH = 10–30%), 3000 atm-cm (RH = 50–60%), 5000 atm-cm (RH = 70–80%), 7000 atm-cm (RH = 90–100%), which included the RH variation in the range of 0–100% 31.

Table 1. Split emission band center of water vapor 33.

Wavenumber (cm^{-1})	7250	5350	3760	1600	140
λ (μm)	1.38	1.87	2.7	6.3	71

Table 2. The calculated ground absolute humidity and TWC for the typical atmospheric model in MODTRAN (2018) 27.

Atmospheric Model	Water column (atm-cm)	Ground Absolute Humidity (g/m^3)
Sub-arctic winter	517.73	1.2113
Mid-latitude winter	1059.7	3.4954
1976 U.S. standard	1762.3	5.8314.
Sub-arctic summer	2589.4	8.9461
Mid-latitude summer	3635.9	13.8255
Tropical	5119.4	18.7574

2.4. Average effective reflectivity and average effective emissivity

Based on the calculation result of the formula and considering the absorption of the atmospheric water vapor, the effective emissivity of the coating was obtained. The performance of the coating was evaluated according to average effective reflectivity $\overline{R}_{solar}$ in solar waveband and average effective emissivity $\overline{\varepsilon}$ in the 'sky window' region. These two parameters were calculated by 40:

$$\overline{R}_{solar}(\theta)=\frac{\int_{0.3\mu m}^{2.5\mu m} I_{solar}(\lambda)R_{solar}(\theta,\lambda)\tau \mathrm{d}\lambda}{\int_{0.3\mu m}^{2.5\mu m} I_{solar}(\lambda)\mathrm{d}\lambda} \tag{12}$$

$$\overline{\varepsilon}=\frac{\int_{8\mu m}^{13\mu m} I_{BB}(T,\lambda)\varepsilon(T,\lambda)\tau \mathrm{d}\lambda}{\int_{8\mu m}^{13\mu m} I_{BB}(T,\lambda)\mathrm{d}\lambda} \tag{13}$$

I_{solar} represented the solar intensity, R_{solar} represented the spectral reflectance, I_{BB} represented the blackbody radiation intensity.

3. Model validation

To verify the accuracy of the algorithm developed to calculate the radiative characteristic by the authors, the computed spectral transmittivity was compared with the values gained by the experimental test. The monodisperse SiO_2 standard microspheres (D_{SiO2} = 284.6 nm) and monodisperse polystyrene (PS) standard microspheres (D_{PS} = 296.5 nm) were selected to compose the multi-particles system for this experiment, where TiO_2 particles were replaced by monodisperse polystyrene standard microspheres due to its inferior monodispersity. SiO_2 and PS standard microsphere solutions were diluted with distilled water to form nanofluids. The volume fractions of SiO_2 and PS standard microspheres in the nanofluids were 0.056% and 0.312%, respectively. A cuvette that optical path length was 1.0 mm was used to keep nanofluids in.

The spectral transmittivity of the nanofluids containing SiO_2 and PS standard microspheres was measured by Ultra-Visible spectrophotometer (TU-1901, Persee, China). According as the effective measuring range of the spectrophotometer was at 400–850 nm wavelengths, the transmittivity of the nanofluids was measured. The related parameters for numerical calculation, such as volume fraction and diameter of the SiO_2 and PS standard microspheres, were based on the above tested values. The complex refractive indexes of SiO_2, PS and H_2O were obtained from Ref. 37. The basic procedures to calculate the transmissivity of the nanofluids by solving the RTE had been presented in Figure 2. As shown in Figure 4, the spectral transmittivity of the diluted microsphere solution computed by the algorithm agreed well with the experimental data at all wavelengths.

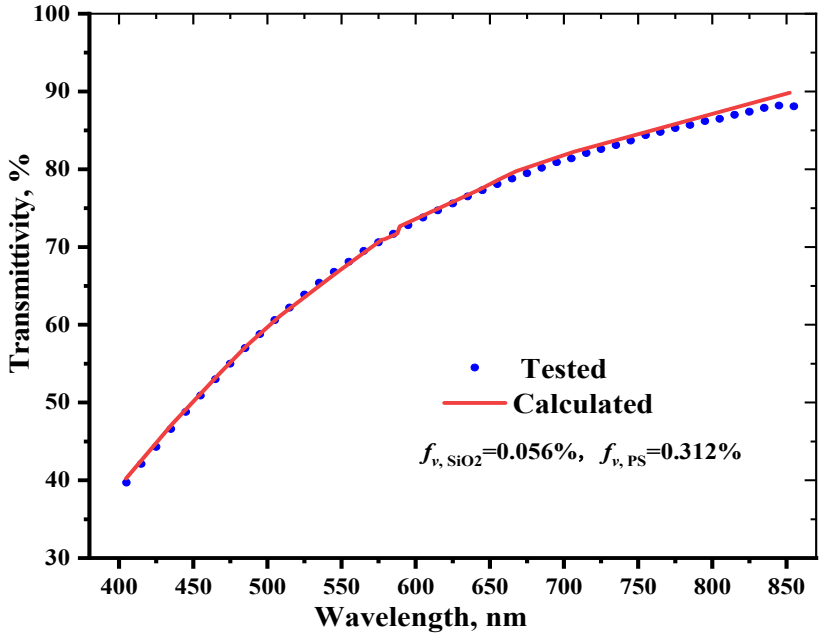

Figure 4. Comparisons of the spectral transmittivity between tested values and calculated results.

4. Results and discussions

4.1. Effects of TWC on atmospheric transmittivity

In this section, Modtran Demo was used to calculate the atmospheric spectral transmittivity at different TWCs, TWC = 0, 1000, 3000, 5000, 7000 atm-cm. Other calculation parameters were kept unchanged: atmosphere model was mid-latitude summer, ground temperature was set as 301 K, aerosol model was urban, spectral range was 0.3–14.0 μm, ozone column value was 0.33176 atm-cm, CO_2 value was 400 ppmv, CO value was 0.15 ppmv, CH_4 value was 1.8 ppmv, the sensor altitude was 50 km 40.

Figure 5 presented the atmospheric spectral transmittivity at different TWCs. As shown in this figure, when the value of TWC was 0 atm-cm, the atmospheric spectral transmittivity was high in both solar waveband and the 'sky window' region. With TWC increasing from 1000 to 7000 atm-cm, the atmospheric spectral transmittivity decreased slightly in solar waveband, while the atmospheric spectral transmittivity decreased significantly in the 'sky window' region. Figure 6 illustrated the atmospheric average transmittivity in solar waveband and "sky window" region at different TWCs., When TWC increased from 0 to 1000 atm-cm, as shown in this figure, the atmospheric average transmissivity in solar waveband dropped rapidly from 75.2% to 64.2% because of the absorption of water vapor. When the values of TWC were 3000, 5000, and 7000 atm-cm, the atmospheric average transmittivity in solar waveband was 59.9%, 57.8%, and 57.2%, respectively. The atmospheric average transmittivity in solar waveband decreased slightly with increasing TWC from 1000 to 7000 atm-cm. In the 'sky window' region, when the value of TWC was 0 atm-cm, the atmospheric average transmittivity was 87.7%. When the values of TWC were 1000, 3000, 5000, and 7000 atm-cm, the average effective transmissivity in the 'sky window' region was 71.2%, 52.0%, 34.1%, and 31.3%, respectively. With the increase of TWC, the atmospheric average transmittivity in the 'sky window' region decreased significantly. It could be concluded from figures that the water vapor had a great influence on the atmospheric average transmittivity, which directly affected the effective emissivity and cooling performance of radiative cooling coatings.

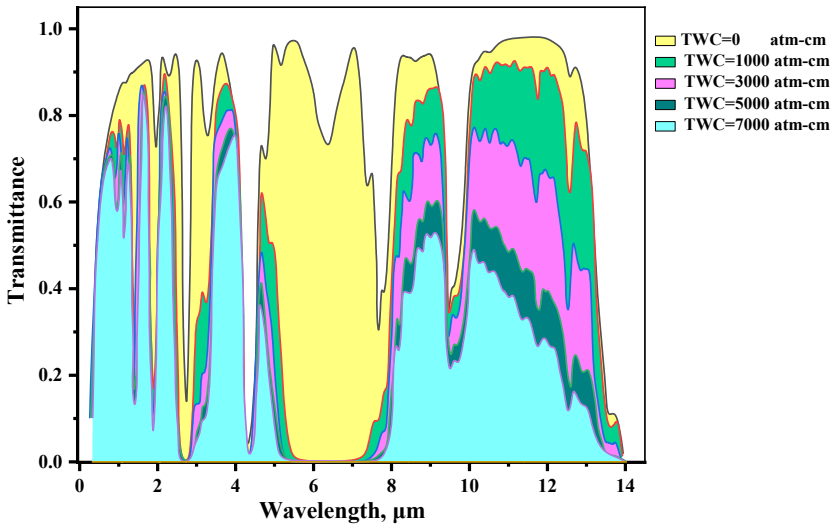

Figure 5. Spectral atmospheric transmittivity at different TWCs.

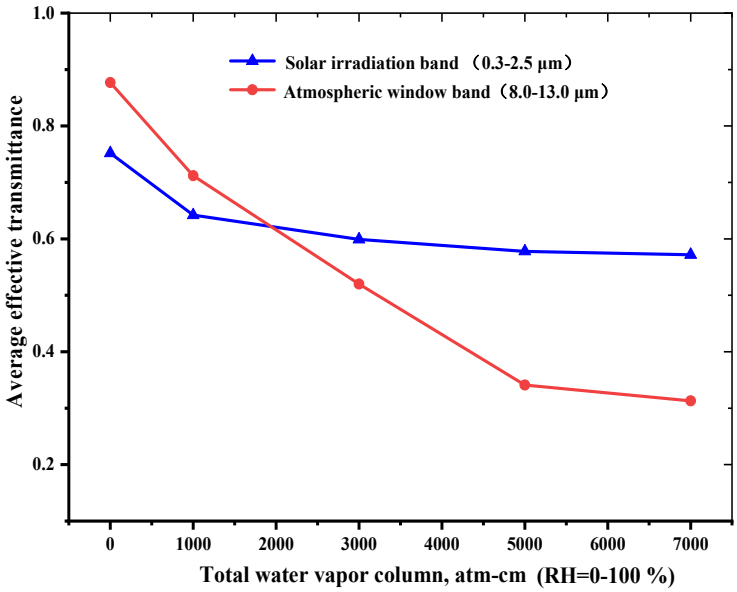

Figure 6. The average transmittivity of the atmosphere in solar waveband and 'sky window' region at different TWCs.

Figure 7 presented the comparison of spectral effective emissivity of the coating with/without consideration of the influence of water vapor, TWC = 0 atm-cm and TWC = 3000 atm-cm. Calculating parameters: volume fractions of SiO_2 and TiO_2 particles were kept the same at 3.0%, while diameters of SiO_2 and TiO_2 particles were kept 4 μm and 0.4 μm unchanged, respectively. The coating thickness was 400 μm. As shown in Figure 7, there were certain differences between TWC = 0 atm-cm and TWC = 3000 atm-cm in all calculated spectrum. At 8.0–13.0 μm wavelengths, the average effective emissivity of the coating at TWC = 0 atm-cm and TWC = 3000 atm-cm was 79.5% and 48.9%, respectively, with a difference of 30.6%. The atmospheric water vapor had a significant influence on effective emissivity of the coatings, so it could not be ignored in the practical application of the coating.

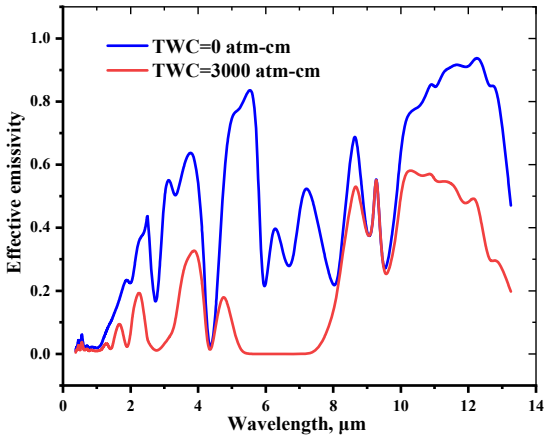

Figure 7. Comparisons of spectral effective emissivity of the coating between the TWC = 0 atm-cm and TWC = 3000 atm-cm.

4.2. The effects of particle diameter at different TWCs

In this section, the spectral effective emissivity of the coating with different the diameters of SiO_2 and TiO_2 particles at different TWCs were studied, respectively. The TWCs were 0, 1000, 3000, 5000, 7000 atm-cm. The diameters of SiO_2 particles were 3.0, 4.0, 5.0, 6.0, 7.0 μm, while the diameters of TiO_2 particles were 0.2, 0.3, 0.4, 0.5, 0.6 μm, respectively. In calculation, the volume fractions of SiO_2 particles and TiO_2 particles were kept $f_{v,SiO2}$ = 2.0% and $f_{v,TiO2}$ = 2.0% unchanged, while the coating thickness was 300 μm [23,42].

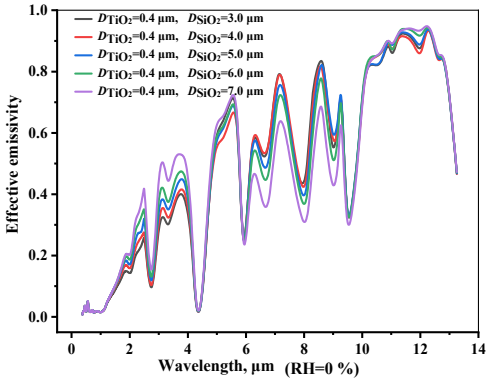

(a) TWC = 0 atm-cm

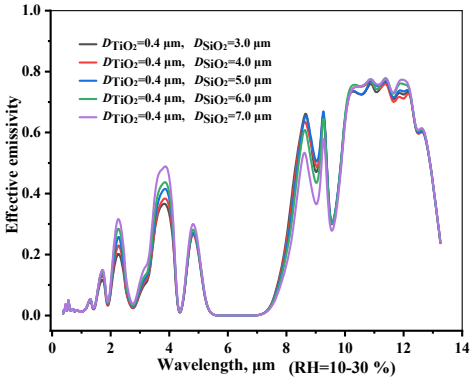

(b) TWC = 1000 atm-cm

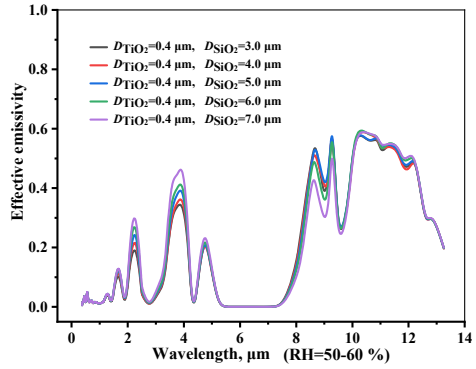

(c) TWC = 3000 atm-cm

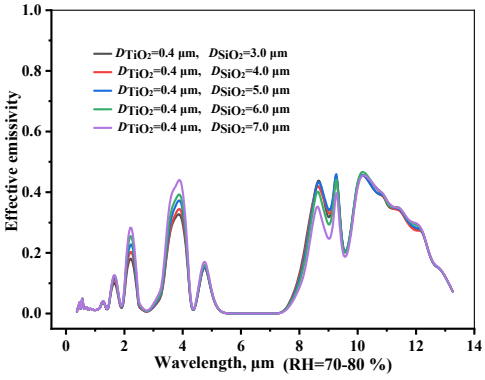

(d) TWC = 5000 atm-cm

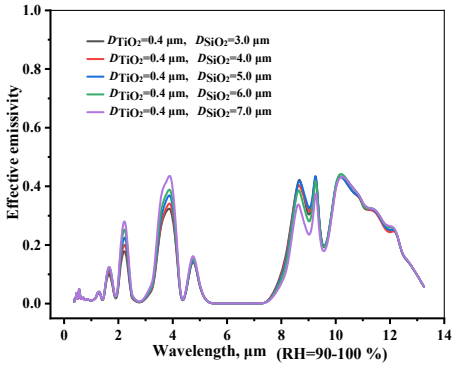

(e) TWC = 7000 atm-cm

Figure 8. Effects of diameters of SiO_2 particles on spectral effective emissivity at different TWCs.

Figure 8 presented the influences of diameters of SiO_2 particles on the spectral effective emissivity of the coating at different TWCs, while D_{TiO2} = 0.4 μm was unchanged. As shown in Figure 8 (a)–(e), as a whole, water vapor had a large influence on the spectral effective emissivity because of its strong absorption in the 'sky window' region. Under the condition of the same diameter of SiO_2 particles, when TWC was within the range of 0–5000 atm-cm, the spectral effective emissivity of the coating decreased sharply with increasing TWC, but the decreasing extent reduced gradually. When TWC was within the range of 5000–7000 atm-cm, the spectral effective emissivity of the coating decreased slowly with increasing TWC. Under the condition of the same TWC, the change trend of the spectral effective emissivity of the coating varied with the diameter of SiO_2 particles was consistent at different TWCs. Taking as an example TWC = 3000 atm-cm, as presented in Figure 8 (c), with increasing the diameter of the SiO_2 particle, the spectral effective emissivity of the coating decreased at 8.0–9.5 μm wavelength, while it increased at 9.5–13.0 μm wavelengths.

In order to evaluate the effects of diameters of SiO_2 particles on radiative cooling performance at different TWCs, the average effective emissivity of the coating at 8.0–13.0 μm wavelengths was calculated and the results were shown in Figure 9. With increasing the diameter of SiO_2 particles, the average effective emissivity of the coating increased first and then decreased at different TWCs. When the SiO_2 particle size was 4.0 μm, the average effective emissivity of the coating at 8.0–13.0 wavelengths reached the highest value. The highest emissivity at this particle size was mainly because resonance occurred to excite higher-order electric and magnetic modes in the 'atmospheric window' spectrum. Besides, the average effective emissivity of the coating decreased with increasing the TWC. Taking for example the D_{SiO2} = 4.0 μm, the average effective emissivity in the 'sky window' region was 74.8% when the value of TWC was 0 atm-cm. The average effective emissivity of the coating at 1000, 3000, 5000 and 7000 atm-cm was 62.0%, 45.8%, 32.8%, 31.6%, respectively, with a decrease of 12.8%, 29.0%, 42.0%, 43.2%. It seriously affected the ability of the coating to emit energy to outer space, which resulted in that cooling effect was not observed in high humidity areas.

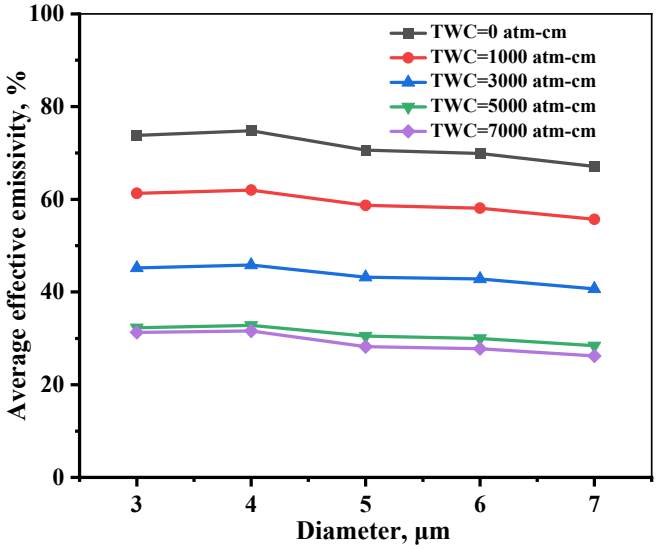

Figure 9. Effects of diameters of SiO_2 particles on the average effective emissivity at different TWCs.

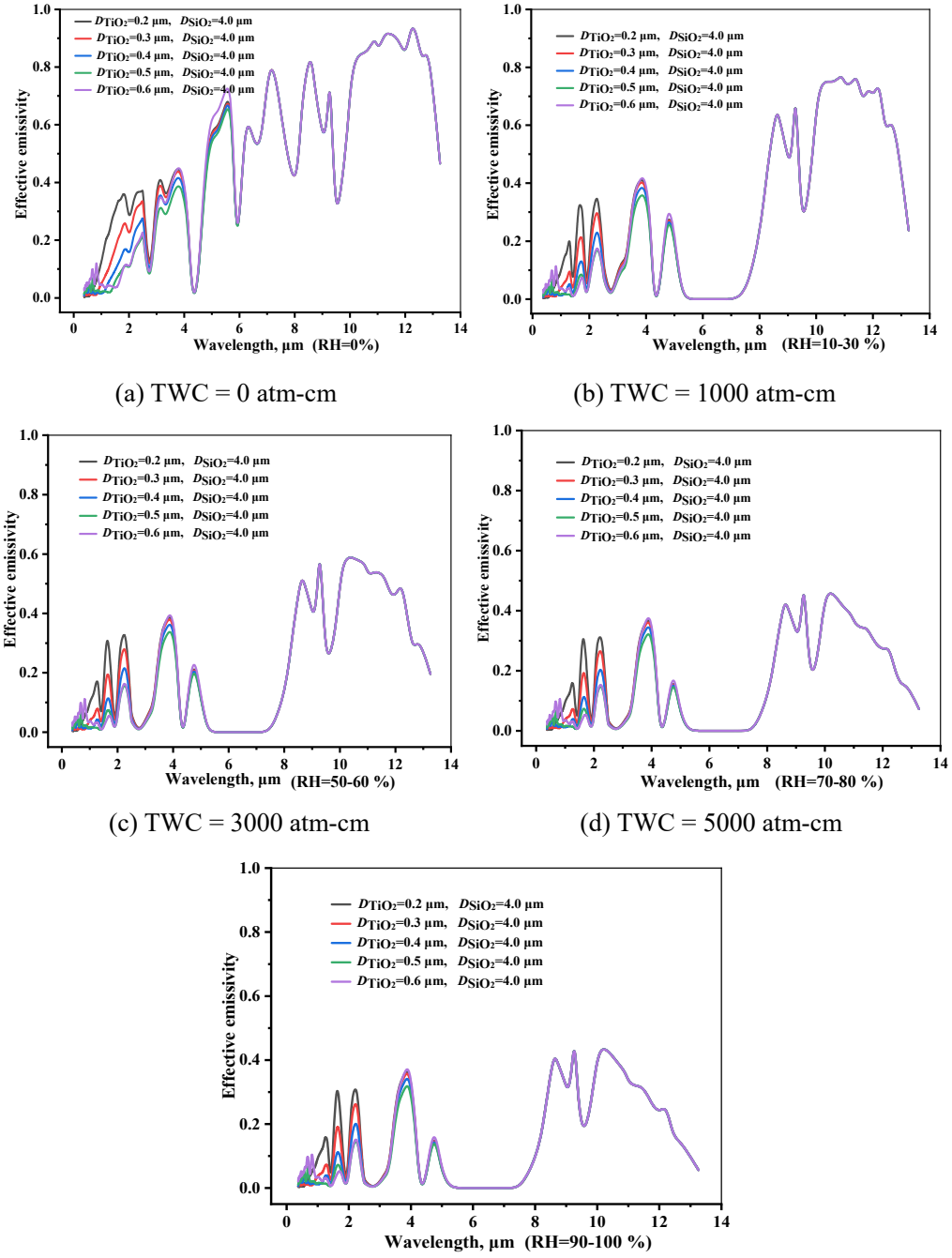

(a) TWC = 0 atm-cm

(b) TWC = 1000 atm-cm

(c) TWC = 3000 atm-cm

(d) TWC = 5000 atm-cm

(e) TWC = 7000 atm-cm

Figure 10. Effects of diameters of TiO_2 particles on the average effective emissivity at different TWCs.

Figure 10 presented the effects of diameters of TiO_2 particles on the spectral effective emissivity of the coating at different TWCs. Compared Figures 8 and 10, it can be seen that the TiO_2 particle had little influence on the spectral effective emissivity at 8–13 μm wavelengths, but affected the spectral emissivity in solar waveband (0.3–2.5 μm). As presented in Figure 10(a),(b), under the condition of the same diameter of TiO_2 particles, when TWC increased from 0 to 1000 atm-cm, the spectral effective emissivity of the coating decreased obviously because the absorption peaks of the

water vapor in solar waveband were 1.38 μm and 1.87 μm. However, when TWC was within the range of 1000–7000 atm-cm, the spectral effective emissivity of the coating showed minor changes with variation of TWC. As presented in Figure 10 (c), taking as an example TWC = 3000 atm-cm, the spectral effective emissivity oscillated with the change of wavelength. This phenomenon was induced due to the reason that TiO_2 particle size was in the strong Mie scattering region at 0.3–0.8 μm wavelengths. With increasing the diameter of TiO_2 particles, the spectral effective emissivity decreased at 0.3–0.8 μm wavelengths, while it increased at 0.8–2.5 μm wavelengths.

The influences of diameters of TiO_2 on the average effective reflectivity (1-absorptivity-transmissivity) of the coating at different TWCs were shown in Figure 11. The average effective reflectivity of the coating first increased and then decreased at different TWCs with increasing the diameter of TiO_2 particles. When the TiO_2 particle size was 0.4 μm, that average effective reflectivity of the coating at all different TWCs can reach the highest value. This was mostly because the TiO_2 with this average particle size was equivalent to the incident wavelength of the sun, which could exert a strong Mie scattering effect. Although the average effective reflectivity of the coating in solar waveband decreased gradually with the increase of TWC, this did not directly affect the cooling performance of the coating because there was no heat exchange process.

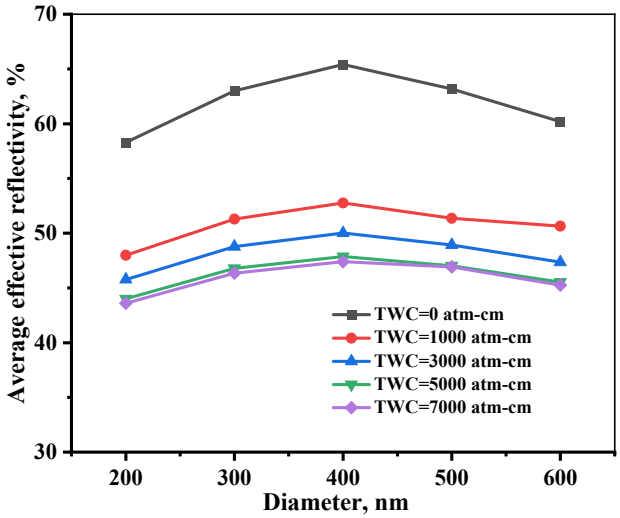

Figure 11. Effects of diameters of TiO_2 particles on the average effective reflectivity of the coating at different TWCs.

4.3. The effects of particle volume fraction at different TWCs

The effects of the volume fraction of SiO_2 and TiO_2 particles on the spectral effective emissivity of the coating at different TWCs were investigated. The TWCs were 0, 1000, 3000, 5000 and 7000 atm-cm, respectively. The volume fractions of both SiO_2 and TiO_2 particles were 0.5%, 1.0%, 2.0%, 3.0%, 4.0%. The diameters of SiO_2 particles and TiO_2 particles were kept D_{SiO2} = 4 μm and D_{TiO2} = 0.4 μm unchanged, while the coating thickness was 300 μm.

Figure 12 showed that the influences of volume fraction of SiO_2 and TiO_2 particles on the spectral effective emissivity of the coating at different TWCs. Under the condition of a certain TWC, the effect of the volume fraction of the SiO_2 and TiO_2 particles on the spectral effective emissivity of

the coating in different waveband was different. When the wavelength was in 0.3–2.5 μm wavelengths, with increasing the volume fraction of SiO_2 and TiO_2 particles, the spectral effective emissivity of the coating decreased firstly and then remained unchanged. On the contrary, when the wavelength was in 8.0–13.0 μm wavelengths, the spectral effective emissivity increased firstly with the increase of the volume fraction of SiO_2 and TiO_2 particles, and it reached a stable state when the volume fraction of SiO_2 and TiO_2 particles was 3.0%. Under the condition of a certain volume fraction of SiO_2 and TiO_2 particles, with increasing TWC from 0 to 7000 atm-cm, the spectral effective emissivity of the coating decreased significantly. Besides, strong absorption of water vapor weakened the influences of particle volume fractions on the spectral effective emissivity of the coating.

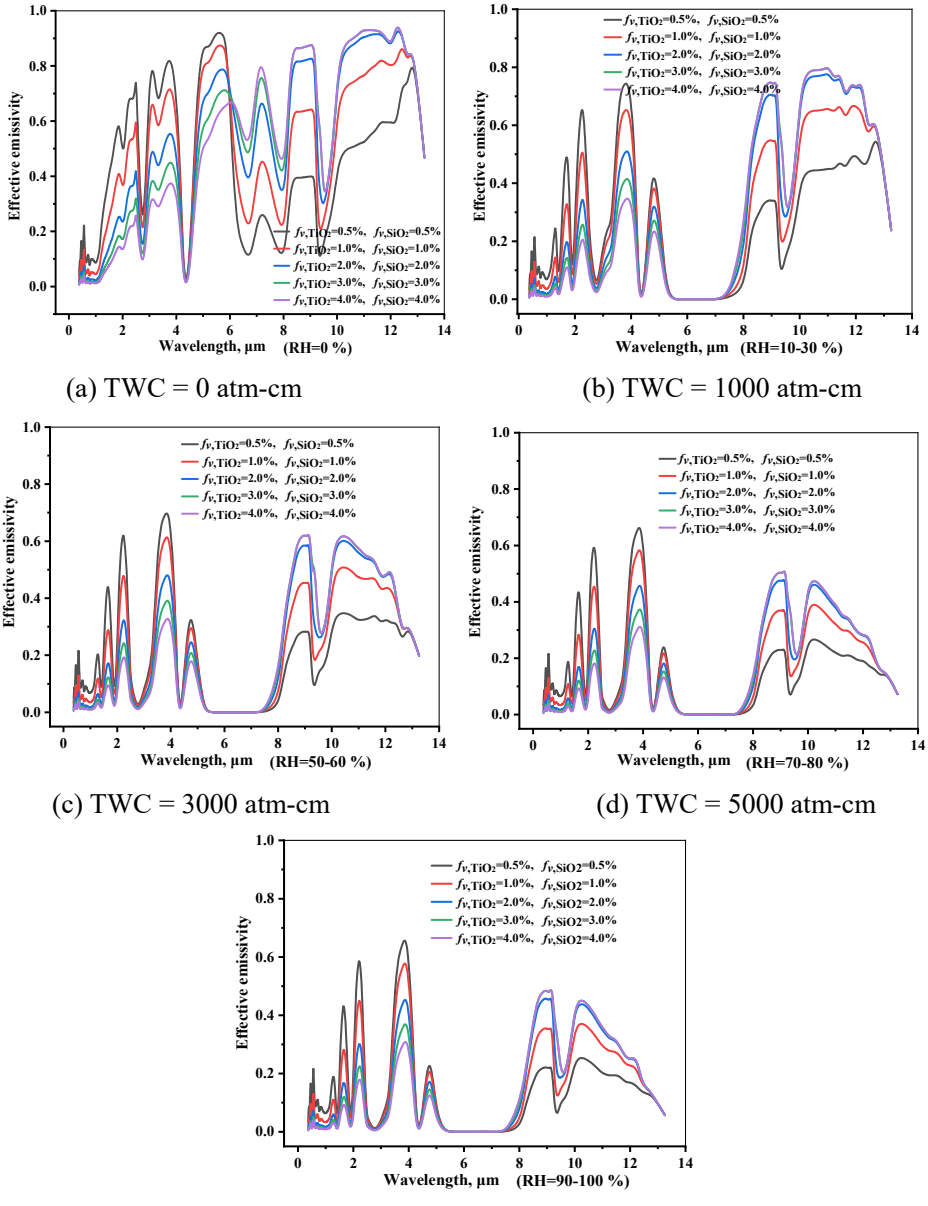

(a) TWC = 0 atm-cm

(b) TWC = 1000 atm-cm

(c) TWC = 3000 atm-cm

(d) TWC = 5000 atm-cm

(e) TWC = 7000 atm-cm

Figure 12. Effects of volume fraction of SiO_2 and TiO_2 particles on the spectral effective emissivity at different TWCs.

Figure 13 presented that the influences of volume fraction of SiO_2 and TiO_2 particles on the average effective emissivity of the coating at different TWCs. As shown in this figure, increasing TWC from 0 to 5000 atm-cm, the average effective emissivity of the coating decreased substantially. The average effective emissivity decreased slightly with increasing TWC when it was in the range of 5000–7000 atm-cm. The average effective emissivity increased first with increasing volume fraction of SiO_2 and TiO_2 particles, and it basically remained unchanged when the volume fraction went up to 3.0%. The main reason for this phenomenon was that the blocking effect of the particles in the coating increased with increasing volume fraction of SiO_2 and TiO_2 particles. Taking the $f_{v,SiO2}$ = 3.0% for example, the average effective emissivity of the coating in the "sky window" region was 75.8% when the value of TWC was 0 atm-cm. The average effective emissivity of the coating at 1000, 3000, 5000 and 7000 atm-cm was 62.9%, 46.6%, 33.1%, 31.9%, respectively, with a relative decrease of 12.9%, 29.2%, 42.7%, 43.9%.

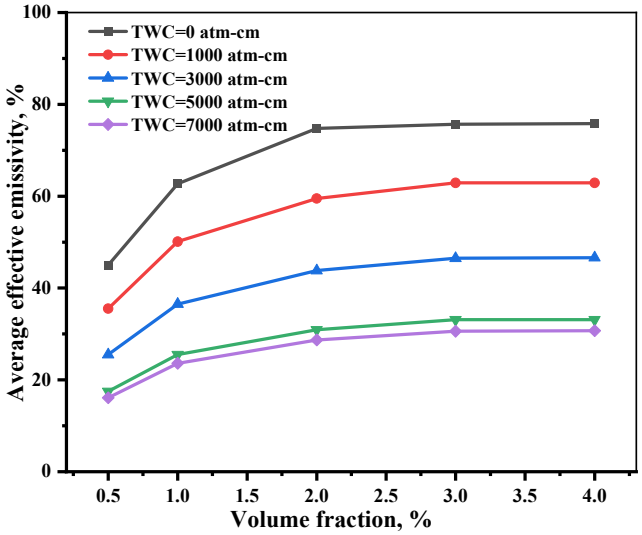

Figure 13. Effects of volume fraction of SiO_2 and TiO_2 particles on the average effective emissivity at different TWCs.

4.4. The effects of coating thickness at different TWCs

In this section, the effects of the coating thicknesses on the spectral effective emissivity of the coating at different TWCs were studied. The TWCs were 0, 1000, 3000, 5000 and 7000 atm-cm, respectively. The coating thicknesses were 250, 300, 350, 400, 450, 500 μm, respectively. The diameters and volume fractions of SiO_2 and TiO_2 particles were the optimal values based on the above calculations.

Figure 14 presented that the influences of coating thicknesses on the spectral effective emissivity of the coating at different TWCs. As shown in Figure 14 (a), when the value of TWC was 0 atm-cm, with the increase of coating thicknesses, the spectral effective emissivity of the coating remained unchanged at 0.3–1.0 μm wavelengths, while it decreased gradually and then basically remained unchanged at 1.0–2.5 μm wavelengths. When TWC was in the range of 1000–7000 atm-cm, it could be seen from Figure 14 (b)–(e) that the spectral effective emissivity of the coating decreased gradually with increasing coating thickness in overall solar waveband. Under

the condition of the different TWCs, the spectral effective emissivity of the coating increased firstly and then remained basically unchanged with increasing coating thickness at 8.0–13.0 μm wavelengths. By comparing Figure 14 (a)–(e), when TWC increased from 0 atm-cm to 7000 atm-cm, the influences of the coating thickness on the spectral effective emissivity were getting weak, and the coating thickness decreased with increasing TWC.

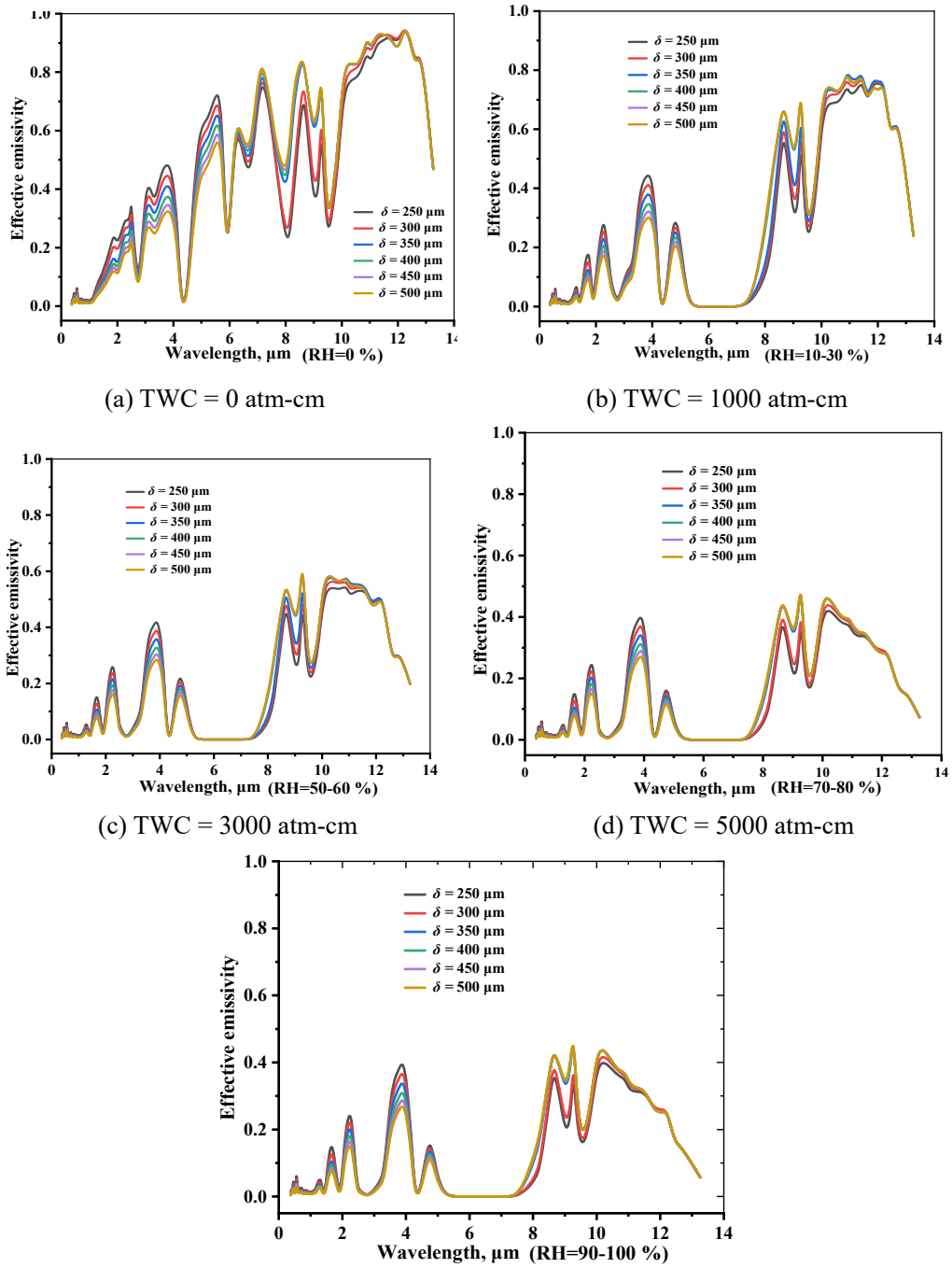

(a) TWC = 0 atm-cm

(b) TWC = 1000 atm-cm

(c) TWC = 3000 atm-cm

(d) TWC = 5000 atm-cm

(e) TWC = 7000 atm-cm

Figure 14. Effects of coating thicknesses on the spectral effective emissivity at different TWCs.

Figure 15 presented that the influences of coating thicknesses on the average effective emissivity of the coating at different TWCs. As shown in this figure, under the condition of the different TWCs, the average effective emissivity of the coating increased first and remained unchanged with the increase of the coating thickness. Taking as an example TWC = 1000 atm-cm, when the coating thickness increased from 250 μm to 400 μm, the average effective emissivity of the coating increased from 60.1% to 66.7%, with an increase of 6.6%. However, with the thickness increased from 400 μm to 500 μm, the average effective emissivity of the coating increased from 66.7% to 67.0%, only increased by 0.3%. As the thickness of the coating increased, the blocking effect of the particles in the coating became more obvious so that the average effective emissivity would not show a high growth rate with increasing coating thickness. When the thickness of the coting was 400 μm, the average effective emissivity of the coating decreased from 79.5% to 35.3% with increasing TWC from 0 to 7000 atm-cm, with a decrease of 44.2%.

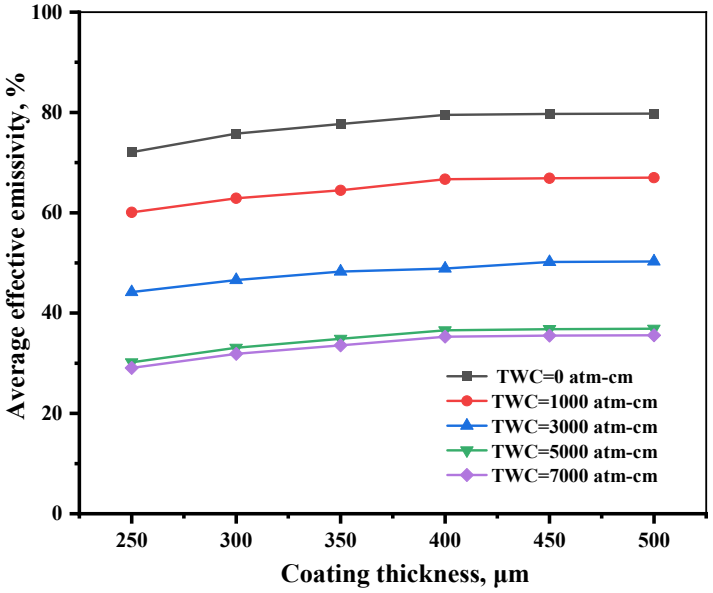

Figure 15. Effects of coating thickness on the average effective emissivity at different TWCs.

5. Conclusions

In this study, taking a simple single-layer radiative cooling coating containing two kinds of particle mixture (SiO_2, TiO_2) as example, the spectral effective emissivity of the radiative cooling coating was proposed to evaluate the effect of the atmospheric water vapor on the cooling performance. The effects of different atmospheric water vapor on the spectral effective emissivity of coating containing different particles size, volume fraction and thickness were studied. Results showed that the influences of the volume fraction of particles and coating thickness on the average spectral effective emissivity were getting weak with the increase of TWC and these two parameters decreased properly. With consideration of the atmospheric water vapor, the simple single-layer radiative cooling coating filled with 5.0% of TiO_2 particles with a diameter of 0.4 μm and 5.5% of SiO_2 with a diameter of 4 μm can obtain the best spectral effective emissivity. Based on the above calculation parameters, with increasing TWC from 0 to 7000 atm-cm, the average effective

emissivity of the coating decreased from 79.5% to 35.3%, with a decrease of 44.2%. This work is of great significance to the further application development and the design criterion of radiative cooling materials in different atmospheric water vapor environments.

Acknowledgements

This work is sponsored by China National Key Research and development Plan Project (Grant No. 2018YFA0702300), Natural Science Foundation of China (Grant No. 51676061), and Taishan Scholars of Shandong Proviance (tsqn201812105).

Conflicts of interest

The authors declare no conflicts.

References

1. Arif MSB, Uvais M, Shahrin BMA (2020) Extensively used conventional and selected advanced maximum power point tracking techniques for solar photovoltaic applications: An overview. *AIMS Energy* 8: 935–958.
2. Tuncbilek E, Arici M, Krajcik M (2020) Thermal performance based optimization of an office wall containing PCM under intermittent cooling operation. *Appl Therm Eng* 179: 115750.
3. Qiu Y, He YL, Li MJ, et al. (2019) Numerical and experimental study on heat transfer and flow features of representative molten salts for energy applications in turbulent tube flow. *Int J Heat Mass Tran* 135: 732–745.
4. Wang K, Zhang ZD, Li MJ, et al. (2020) A coupled optical-thermal-fluid-mechanical analysis of parabolic trough solar receivers using supercritical CO_2 as heat transfer fluid. *Appl Therm Eng* 183: 116154.
5. Kasaeian A, Bellos E, Shamaeizadeh A (2020) Solar-driven polygeneration systems: Recent progress and outlook. *Appl Energ* 264: 114764.
6. Zhang K, Zhao D, Zhai Y, et al. (2017) Modelling study of the low-pump-power demand constructal T-shaped pipe network for a large scale radiative cooled-cold storage system. *Appl Therm Eng* 127: 1564–1573.
7. Feng J, Santamouris M (2019) Numerical techniques for electromagnetic simulation of daytime radiative cooling: A review. *AIMS Mater Sci* 6: 1049.
8. Han D, Ng BF, Wan MP (2020) Preliminary study of passive radiative cooling under Singapore's tropical climate. *Sol Energ Mat Sol C* 206: 110270.
9. Shen D, Yu C, Wang W (2020) Investigation on the thermal performance of the novel phase change materials wall with radiative cooling. *Appl Therm Eng* 176: 115479.
10. Hu MK, Pei G, Wang Q, et al. (2016) Field test and preliminary analysis of a combined diurnal solar heating and nocturnal radiative cooling system. *Appl Energ* 179: 899–908.
11. Cheng ZM, Wang FQ, Gong DY, et al. (2020) Low-cost radiative cooling blade coating with ultrahigh visible light transmittivity and emission within an ‘atmospheric window’. *Sol Energ Mat Sol C* 213: 110563.

12. Xu ZK, Li N, Liu DF (2018) A new crystal $Mg_{11}(HPO_3)_8(OH)_6$ for daytime radiative cooling. *Sol Energ Mat Sol C* 185: 536–541.
13. Gentle AR, Smith GB (2010) Radiative heat pumping from the Earth using surface phonon resonant nanoparticles. *Nano Lett* 10: 373–379.
14. Wu XH, Fu CJ, Zhang ZM (2020) Chiral absorbers based on polarization conversion and excitation of magnetic polaritons. *ES Energ Environ* 8: 5–14.
15. Zhao B, Hu MK, Ao XZ, et al. (2019) A novel strategy for a building-integrated diurnal photovoltaic and all-day radiative cooling system. *Energy* 183: 892–900.
16. Cheng ZM, Wang FQ, Wang H (2019) Effect of embedded polydisperse glass microspheres on radiative cooling of a coating. *Int J Therm Sci* 140: 358–367.
17. Fan JS, Fu CJ, Fu TR (2020) Yttria-stabilized zirconia coating for passive daytime radiative cooling in humid environment. *Appl Therm Eng* 165: 114585.
18. Bao H, Yan C, Wang B (2017) Double-layer nanoparticle-based coatings for efficient terrestrial radiative cooling. *Sol Energ Mat Sol C* 168: 78–84.
19. Fan DS, Sun H, Li Q (2019) Thermal control properties of radiative cooling foil based on transparent fluorinated polyimide. *Sol Energ Mat Sol C* 195: 250–257.
20. Chai JL, Cheng Q, Si M (2017) Numerical simulation of white double-layer coating with different submicron particles on the spectral reflectance. *J Quant Spectrosc Ra* 189: 176–180.
21. Raman AP, Anoma MA, Zhu L (2014) Passive radiative cooling below ambient air temperature under direct sunlight. *Nature* 515: 540–544.
22. Cheng ZM, Shuai Y, Gong DY, et al. (2020) Optical properties and cooling performance analyses of single-layer radiative cooling coating with mixture of TiO_2 particles and SiO_2 particles. *Sci China Technol Sc* 63: 1–13.
23. Huang ZF, Ruan XL (2017) Nanoparticle embedded double-layer coating for daytime radiative cooling. *Int J Heat Mass Tran* 104: 890–896.
24. Feng J, Gao K, Santamouris M, et al. (2020) Dynamic impact of climate on the performance of daytime radiative cooling materials. *Sol Energ Mat Sol C* 208: 110426.
25. Qi H, Wen S, Wang YF, et al. (2019) Real-time reconstruction of the time-dependent heat flux and temperature distribution in participating media by using the Kalman filtering technique. *Appl Therm Eng* 157: 113667.
26. He MJ, Qi H, Ren YT, et al. (2020) Magnetoplasmonic manipulation of nanoscale thermal radiation using twisted graphene gratings. *Int J Heat Mass Tran* 150: 119305.
27. Liu C, Wu Y, Wang B, et al. (2019) Effect of atmospheric water vapor on radiative cooling performance of different surfaces. *Sol Energ* 183: 218–225.
28. Zhai Y, Ma Y, David SN, et al. (2017) Scalable-manufactured randomized glass-polymer hybrid metamaterial for daytime radiative cooling. *Science* 355: 1062–1066.
29. Zhao D, Aili A, Zhai Y, et al. (2019) Subambient cooling of water: Toward real-world applications of daytime radiative cooling. *Joule* 3: 111–123.
30. Mandal J, Fu Y, Overvig AC (2018) Hierarchically porous polymer coatings for highly efficient passive daytime radiative cooling. *Science* 362: 315–319.
31. Liu J, Zhang D, Jiao S, et al. (2020) Preliminary study of radiative cooling in cooling season of the humid coastal area. *Sol Energ Mat Sol C* 208: 110412.

32. Li MY, Coimbra CFM (2019) On the effective spectral emissivity of clear skies and the radiative cooling potential of selectively designed materials. *Int J Heat Mass Tran* 135: 1053–1062.
33. Modest M (2013) Radiative Heat Transfer, 3rd Edition, San Diego: Academic Press.
34. Liu BK, Zhao JM, Liu LH (2020) Continuum approach based on radiation distribution function for radiative heat transfer in densely packed particulate system. *J Quant Spectrosc Ra* 253: 107028.
35. Ma LX, Wang CC, Tan JY (2019) Light scattering by densely packed optically soft particle systems with consideration of the particle agglomeration and dependent scattering. *Appl Optics* 58: 7336–7345.
36. Wang FQ, Wang H, Gong DY (2019) Radiative transfer analysis of semitransparent medium with particles having non-uniform size distribution by differential-integration method. *Int J Heat Mass Tran* 130: 342–355.
37. Palik ED (1985) Handbook of Optical Constants of Solids, San Diego: Academic Press.
38. Tan JY, Xie YM, Wang FQ, et al. (2017). Investigation of optical properties and radiative transfer of TiO_2 nanofluids with the consideration of scattering effects. *Int J Heat Mass Tran* 115: 1103–1112.
39. Reber EE, Swope JR (1972) On the correlation of the total precipitable water in a vertical column and absolute humidity at the surface. *J Appl Meteorol Clim* 11: 1322–1325.
40. MODTRAN Demo Available from: http://modtran.spectral.com/modtran_home#plot.
41. Cheng ZM, Shuai Y, Gong DY, et al. (2020) Optical properties and cooling performance analyses of single-layer radiative cooling coating with mixture of TiO_2 particles and SiO_2 particles. *Sci China Technol Sc* 63: 1–13.
42. Peoples J, Li X, Lv Y, et al. (2019) A strategy of hierarchical particle sizes in nanoparticle composite for enhancing solar reflection. *Int J Heat Mass Tran* 131: 487–494.

AIMS Press